Partially Erupted Prominence Material as a Diagnostic of Coronal Mass Ejection Trajectory

B.A. Hovis-Afflerbach[1,2,3], B.J. Thompson[2], E.I. Mason[4]

[1]California Institute of Technology, Pasadena, CA, USA
[2]NASA Goddard Space Flight Center, Greenbelt, MD, USA
[3]Catholic University of America, Washington, DC, USA
[4]Predictive Science Inc., San Diego, CA, USA

Key Points:

- We examine the motion of partially erupted prominence material and coronal mass ejection (CME) relative to eruptive source location
- We find a correlation between the offsets in latitude from the source location
- Partially erupted prominence material can be a predictor of CME direction relative to source region and highlight evolving magnetic topology

Corresponding author: Beryl Hovis-Afflerbach, `berylha@caltech.edu`

Abstract

Coronal mass ejections (CMEs) are energetic releases of large-scale magnetic structures from the Sun. CMEs can have impacts on spacecraft and at Earth. This trajectory is typically assumed to be radial, but often the CME moves outward with some spatial offset from the source region where the eruption initially occurred. A CME is frequently accompanied by a prominence eruption, a movement of cool, dense material up into the corona that can be ejected or fall back down. We investigate eruptions in which some portion of the prominence material falls back to the Sun along field lines which have reconfigured in the eruption, rather than draining back to the source or escaping with the CME. Using a method called persistence mapping, 304 Å images from the *Solar Dynamics Observatory* (SDO), and coronagraph images from the *Solar and Heliospheric Observatory* (SOHO), we measure and compare the offsets in latitude of 20 CMEs and their respective prominences with respect to the source region. The 20 events were chosen to sample over the first 10 years of the SDO mission. We find that the offsets are correlated. We find no difference between eruptions offset towards the equator or the poles, suggesting that the offset is a result of local changes in the eruptive field, rather than of the Sun's global magnetic field structure. These findings help us contextualize individual eruptions and highlight changes in the local magnetic field associated with the prominence eruption.

Plain Language Summary

Solar eruptions can have impacts on spacecraft and at Earth. We investigate two components of solar eruptions: the coronal mass ejection (CME), which is an energetic release of large-scale magnetic structure from the Sun, and partially erupted prominence material (PEPM) that falls back to the Sun along changing magnetic field lines during the eruption. For multiple eruptions, we measure and compare the offset in latitude of both the CME and PEPM from the source region where the eruption originated. We find that the two offsets are correlated, indicating that the changing magnetic field topology impacts both of these components. These findings can help us contextualize individual eruptions and highlight the changing local magnetic field.

1 Introduction

A solar eruption occurs when there is an energetic release of a large-scale magnetic structure from the Sun. Eruptions are often characterized by a flare, which is an emission of light ranging in frequency from radio to gamma rays, a prominence, which is a movement of cool, dense material up into the corona that can either be ejected from the Sun or fall back down, and/or a coronal mass ejection (CME), which is observed as a large volume of material that successfully escapes from the Sun.

Space weather forecasters use the eruption source location on the Sun to inform an initial guess for the CME trajectory, especially in cases in which the CME shows up faint in coronagraph imagery and is difficult to measure using typical tools. Given the significant impacts that CMEs can have at Earth, accurate forecasting, especially early, is very important. In many cases, the eruption does not simply move radially from the observed source region where the prominence material first emerged; very often there is some offset of the CME trajectory from the source. Therefore, source coordinates alone are not an accurate prediction of CME trajectory.

Approximately 72% (Gopalswamy et al., 2003) of prominence eruptions are associated with CMEs. Because prominences are dense material embedded in a CME's magnetic field, they are often transported away from the Sun during an eruption. Their connection to CME topology and kinematics provides important information about the eruptive process (Gilbert et al., 2000).

However, in a typical eruption, at least a portion of the prominence material is observed to "drain" back down to the eruption's source region (van Ballegooijen & Martens, 1989; Schmieder et al., 2013). Additionally, in some cases a significant portion of the material is observed to fall back to the Sun, landing in a location significantly displaced from the eruption's source. This phenomenon has been called by some "partial" or "failed" eruptions, in that the material that was initially rising fails to escape the Sun and enter the solar wind (Ji et al., 2003; Tripathi et al., 2013; Filippov, 2020; Mason et al., 2021). The material that falls back follows magnetic field lines, which have changed during the course of the eruption. The location of the partially erupted prominence material (PEPM) outside of the source region reveals clues about the changing magnetic field structure of a solar eruption and provide diagnostics about the larger-scale topology of the associated CME (Susino et al., 2014; Uritsky et al., 2022).

Uritsky et al. (2022) demonstrated how falling prominence material can be used as a diagnostic of the magnetic forces on the plasma during and after an eruption. They tracked the motion of the material from the source site, and measured the trajectories of the individual blobs. The eruption they used in this analysis is one of the events in our study (2011-06-07). They determined that the falling material can serve as an indicator of changing coronal magnetic forces during a coronal mass ejection. The initial acceleration of material was confined to the flaring source region. However, as the CME expanded and rose, most of the material was accelerated away from the source and landed at locations distant from the erupting site. Several authors (van Driel-Gesztelyi et al., 2014; Petralia et al., 2016; Dudík et al., 2019) used the modeled magnetic field and plasma motion to infer changes in the magnetic connectivity of the coronal field due to reconnection from the eruption. They demonstrated how the moving material, and the regions of the corona that it now can access, can form a more complete picture of the extent of the magnetic fields that evolve during the CME.

The analysis presented in this paper extends those results by addressing the question of how one aspect of the evolving topology at the base of a CME, in the form of falling material away from the source site, compares to the overall CME's structure and trajectory. In particular, we ask whether material's behavior at the bottom can be used as an indicator of the CME's extent as observed in coronagraph data.

To attempt to answer these questions, we compare how the latitude of an eruption's PEPM and CME compare and change over the course of an eruption and investigate the changing magnetic field conditions associated with these eruptions. In § 2, we describe how we selected a set of eruptions for this study, the data we used, and the process by which we made our measurements. In § 3, we present our findings on the correlation between the motion of the PEPM and CME, as well as how the CME evolves over time. In § 4, we discuss the implications of these findings and what they reveal about the eruptive magnetic field. In § 5, we summarize the results and implications.

2 Methods

In this section we describe how we found and selected solar eruptions for this study, as well as the data we used for our measurements (§ 2.1). We then describe how we made measurements of each eruption's latitude in source (§ 2.2), PEPM (§ 2.3), and CME (§ 2.4).

2.1 Selection of prominence eruptions and data

In our initial search for eruptions, we looked through the *Space Weather Database Of Notifications, Knowledge, Information* (DONKI; Wold et al., 2018) from the *Community Coordinated Modeling Center* (CCMC). This database contains a record of all observations of CMEs made by space weather forecasters since 2010, as well as measurements of each CME's latitude, longitude, width, and speed for fast ($>$ 500 km/s) CMEs in the plane of the ecliptic. Because these measurements were made limited to data available at the time of the forecast, often inferred from only a few data points, and for different CMEs were made by different forecasters with varying levels of experience, we made our own measurements for each CME; we used DONKI only to find events to measure. We selected only eruptions that occurred since the *Solar Dynamics Observatory* (SDO; Pesnell, Thompson, & Chamberlin, 2012) began regular observations in May 2010 and that had full coverage in both of the instruments we use: the *Atmospheric Imaging Assembly* (AIA; Lemen et al., 2012) onboard SDO and the *Large Angle and Spectrometric Coronagraph* (LASCO; Brueckner et al., 1995) onboard the *Solar and Heliospheric Observatory* (SOHO; Domingo, Fleck, & Poland, 1995). To ensure that we would be able to easily observe and accurately measure the eruption in a plane-of-sky image, we narrowed our search to eruptions in which the CME was measured in DONKI to be only $\pm 10°$ from the limb, $\pm 90°$ of longitude. We considered CMEs where in DONKI the description mentioned a prominence or filament in the source description and selected events that had clearly visible PEPM. Specifically, we looked at AIA images in 304 Å to determine for which events the falling material is offset from the source of the eruption, indicating that the magnetic field topology clearly changes, rather than those in which the material drains back along the same field lines that were present prior to the eruption. The sample is somewhat arbitrary in that it was a function of the DONKI observer's notes and was also dependent on the clear appearance of the PEPM in the summary movies, which were much lower cadence than that data used to analyze the PEPM. Therefore, the DONKI database and summary data were systematically searched, but our sample does not contain all of the events that would be found in a high-cadence examination of all AIA images. Table 2 lists all events used in this study.

For each eruption chosen, we noted whether it was from an active region. These regions have more complex magnetic field topology, are bright in EUV wavelengths, and are designated as active regions and numbered by NOAA. We selected 20 eruptions in total, 14 of which erupted from active regions and 6 of which came from "quiet Sun" regions, where the magnetic field is weaker. The prominence eruptions varied in duration, lasting between 1.5 and 6.5 hours.

For each event, we downloaded SDO AIA data from the *Joint Science Operations Center* (JSOC) database for the full time range in 304Å, a He II emission line at around 50,000 K, as well as in 193Å, emission lines of Fe XII and Fe XXIV at around 1 million K and 20 million K, respectively. The cadence was selected such that there were a similar number of frames used for each eruption. There were typically $\sim$ 300 frames per event.

2.2 Source measurement

To measure the northern and southern bounds of the source region, we used the `Map` object from the python package SunPy (SunPy Community et al., 2020) to load one frame during the eruption from the data we downloaded in 304Å. We looked at a movie of the full eruption to determine which frame best shows the beginning of the eruption, when there was a sudden noticeable change from the ambient conditions, which we used to pinpoint the source region. We then plotted this frame interactively using the `canvas.mpl_connect` function from the matplotlib package, which we set up such that when we clicked somewhere on the image, the pixel position of the click is recorded. This position was then converted from a pixel coordinate to a heliographic longitude and latitude using SunPy's `pixel_to_world` function and printed as an output, which we recorded. We defined the uncertainty in the source measurement as approximately 10 pixels at equatorial locations. This means that in degrees, the latitude-dependent uncertainty of each measurement is $0.358°/\cos\theta$, where θ is the latitude measured. All our uncertainties in raw measurement came out to be $\leq 1°$. Using this method, we determined the latitude of the northern and southern bounds of the source region at the level of the chromosphere for each eruption.

2.3 Prominence measurement

Persistence Mapping, first described by Thompson and Young (2016), is a technique for capturing the evolution of a feature over the course of time and representing it in a single diagram. It has been used to study the motion of EUV jets (McCauley et al., 2017), coronal dimmings (Dissauer et al., 2018), EUV waves (Ireland et al., 2019), and prominence eruptions (Zheng et al., 2020). In this work, we used it to investigate the evolution of prominence eruptions, specifically of PEPM that falls back to the Sun.

The persistence mapping algorithm iterates through EUV images of the eruption in AIA 304 Å. When a pixel reaches a maximum value, it retains that value, so extreme values persist into subsequent image frames until those values are exceeded. The brightness of the pixel indicates the degree of change. Darker pixels did not exhibit much change, while bright pixels exhibited a great deal of change. This helps us to distinguish noise and ambient variations from major changes associated with the prominence evolution.

Here, we also use a variation on persistence mapping to add time data to the image, described by Mays et al. (2015) as the "Time Convolution Mapping Method" (TCMM). In this variation, when a pixel reaches a maximum value, it retains that value and is colored by the time when it reached that maximum. The brightness of the pixel is convolved with the color code, so that bright regions have a bright hue and faint regions in the persistence map remain faint in the TCMM map. The product reflects four values: two dimensions for space, color code for time, and brightness for intensity.

Persistence maps allow us to easily see and measure the extent of the PEPM and allow us to better trace PEPM and therefore the changing magnetic field. A comparison of original images, persistence maps, and time convolution maps for a prominence eruption on 2012-04-22 are shown in Figure 1. Three examples of the result of time convolution mapping are shown in Figure 2.

For each eruption, after creating a persistence map, we opened it as a SunPy map like we did for the source measurement and used the same interactive plotting function to determine the northern and southern bounds of the PEPM footprints in heliographic latitude. We used a frame at the end of the prominence eruption, so that the full range of prominence motion is included in the persistence map. We determined the PEPM measurement uncertainty in the same way as we did for the source measurement.

2.4 CME measurement

To make measurements of the northern and southern bounds of the CME, we used StereoCAT, a tool for measuring CMEs using coronagraph data from the SOHO and *Solar Terrestrial Relations Observatory* (STEREO) spacecraft. For this work, we only used the data from SOHO, as it is located at the Sun-Earth L1 Lagrange point and takes images of the Sun from Earth's field of view. Because we have selected only eruptions that occur on or close to the solar limb, plane of sky measurements from this one telescope are sufficient to measure the latitude of the CME. We do not extend this study to longitude because three-dimensional measurements of CMEs require geometric assumptions and well-positioned measurements from multiple spacecraft. The error associated with longitude determination of both the CME and prominence makes the study less reliable in three dimensions.

We measured the northern and southern bounds of the CME latitude as projected onto the Sun in LASCO's C2 and C3 fields, which extend to 6 $R_\odot$ and 30 $R_\odot$, respectively, so that we measure the CME at two different times in its progression. All three

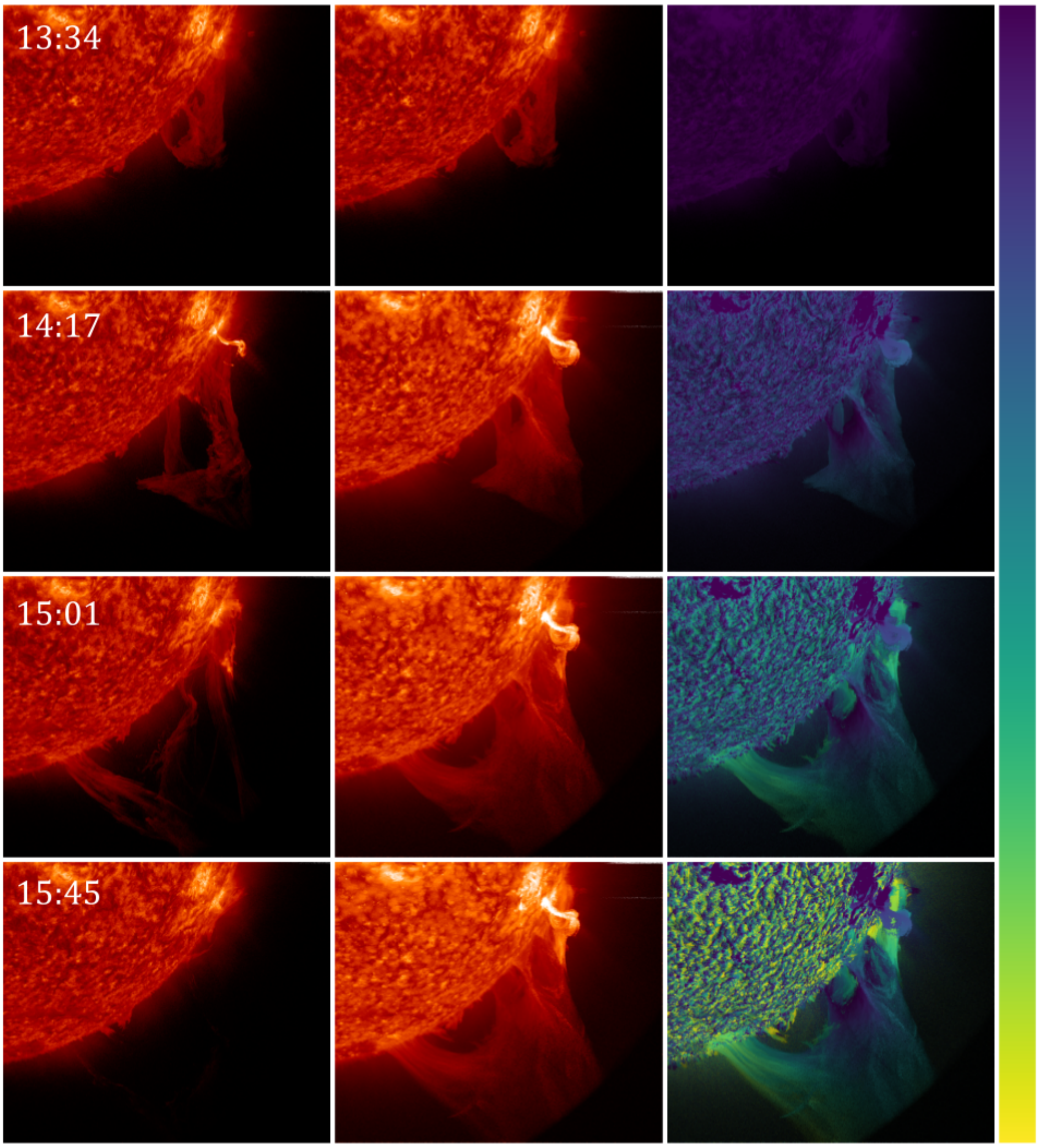

Figure 1. Prominence eruption on 2012-04-22 as seen in SDO AIA 304 Å. Original images (left), persistence map (center), and Time Convolution Map, which is a persistence map colored by time at which each pixel reaches its greatest intensity (right). By the end of the prominence eruption in the last image frame, there is no clear sign of the prominence in the original image. However, the persistence maps retain the time history of the prominence eruption. The full eruption lasts 2 hours 11 minutes, with 44 minutes between each frame shown. Dark purple designates the beginning of the eruption at 13:34, lighter purple designates 14:17, green shows 15:01, and yellow signifies the end of the eruption at 15:45.

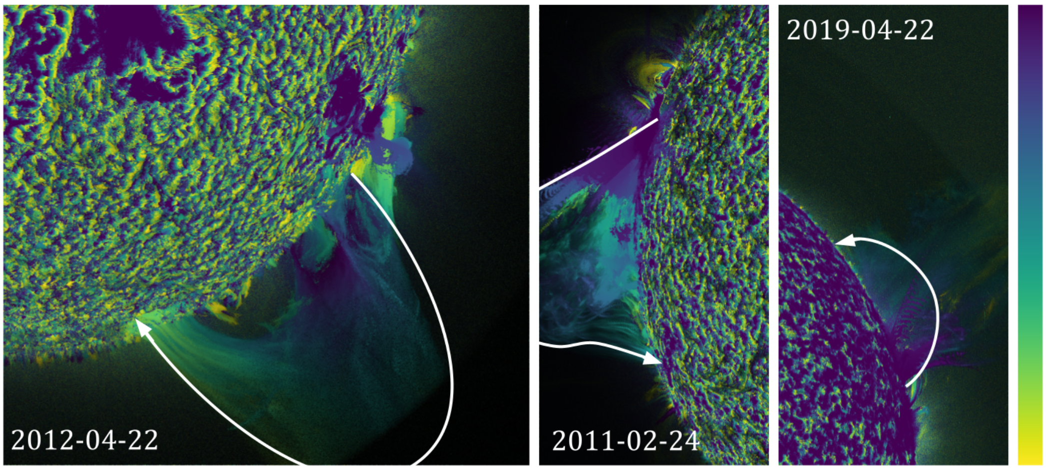

Figure 2. Persistence maps of prominence eruptions on 2012-04-22, 2011-02-24, and 2019-04-22 as seen in SDO AIA 304 Å. The colorbar at right denotes time, beginning with dark purple and ending with bright yellow. The eruptions lasted 2 hours 11 minutes, 2 hours 7 minutes, and 1 hour 11 minutes, respectively. The arrow in each image denotes the motion of the PEPM.

authors independently measured the northern and southern bounds of the main loop structure of each CME at the same point in its progression. We use a single frame in C2 and a single frame in C3. In C2, the measurement time was chosen such that the CME was close to 6 $R_\odot$ from solar disk center, and in C3, the measurement time was chosen such that the CME was close to 15 $R_\odot$ from the center. For the northern and southern bounds of each CME in C2 and C3, we calculated the average and standard deviation of the three measurements. The eruptions that took place on 2015-04-28 and 2019-04-22 were too faint in the outer corona to measure in C3. We therefore excluded these events from Figure 5 and used the measurement taken in the C2 field for Figure 4.

3 Results

In this section we present the results of our measurements. We compare the CME's positional offset in latitude from the source with the PEPM's offset from the source (§ 3.1). We then investigate how this offset continues into the corona as the CME propagates outward (§ 3.2).

3.1 Comparing CME and PEPM offset

We compared the offset in latitude of the CME from the source with the offset of the PEPM from the source. By first taking the mean of the northern and southern bounds then subtracting the latitude of the source from the latitudes of the CME and PEPM, we determined the CME and PEPM offsets. The offset is assigned a negative sign if the CME or PEPM is closer to the equator than the source, and it is assigned a positive sign if it is offset towards the pole.

To better investigate how different types of eruptions proceed and how the magnetic field evolves over the course of the eruption, we grouped eruptions with PEPM into three types, shown in Figure 3 as idealized representations and examples.

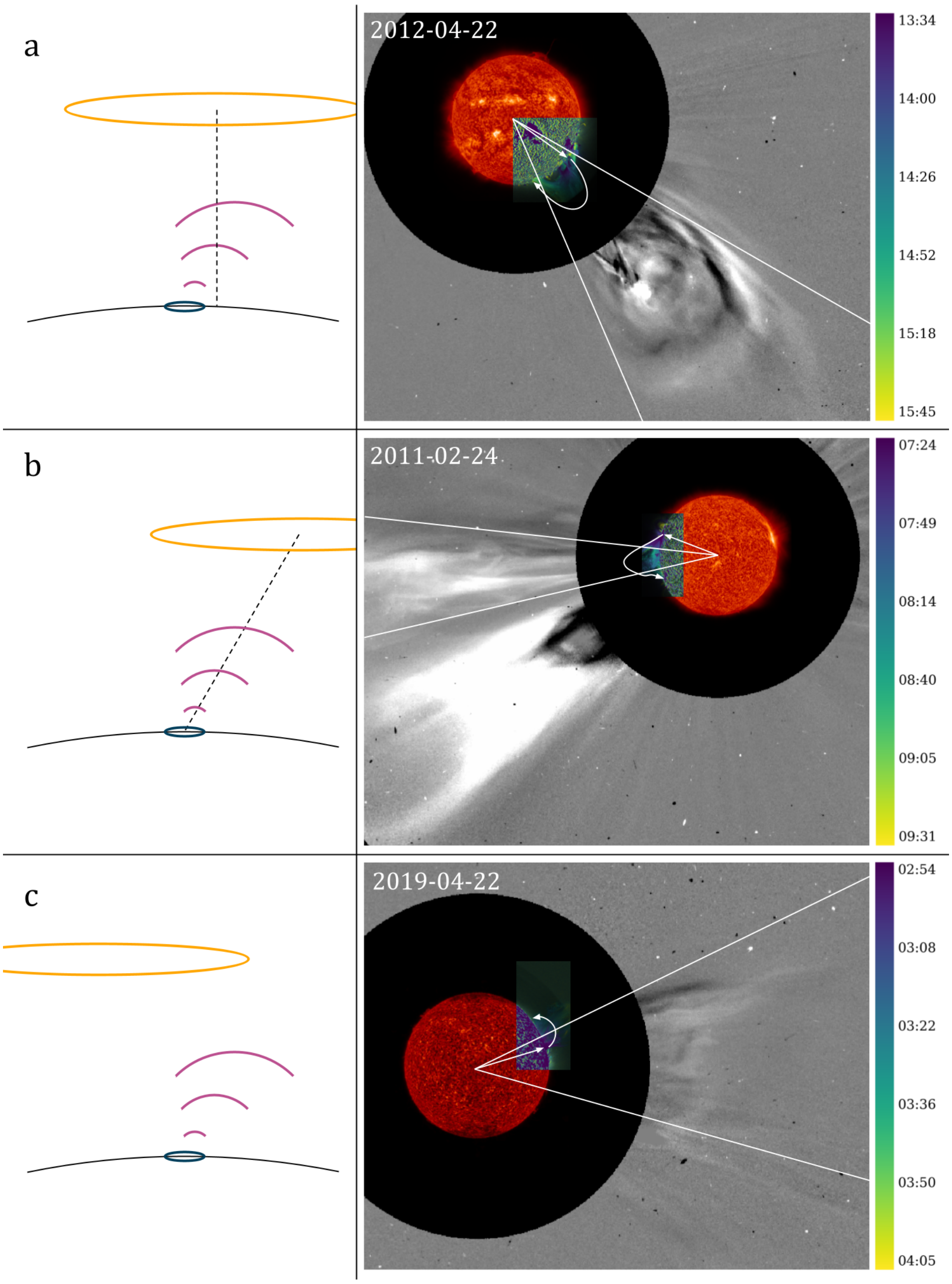

Figure 3. Idealized representations (left) and examples (right) of three possible outcomes for falling prominence eruptions. The left shows the idealized progression from source (blue) to prominence (pink) to CME (orange). The right shows the SOHO LASCO C2 difference image, SDO AIA 304 Å full Sun image, and the persistence map from Figure 2 showing the prominence motion, with a colorbar at far right. The example images have an arrow pointing from solar center to the source, a second arrow showing the PEPM, and two lines denoting the CME plane of sky width. The three types of eruptions examined are (a) CME offset in the same direction as the PEPM but to a lesser extent, (b) progression in offset from PEPM to CME, and (c) PEPM and CME offset in different directions.

Type (a) are eruptions where the CME is offset in the same direction as the PEPM but its offset is less than that of the PEPM. The example shown is from 2012-04-22, where the PEPM is offset to the South and the CME is also offset to the South.

Type (b) are eruptions where the CME is offset in the same direction as the PEPM, and its offset is greater than that of the PEPM, so that there is a progression from source to PEPM to CME. The example shown is from 2011-02-24, where the PEPM is offset to the South and the CME is offset even further South.

Type (c) are eruptions where the PEPM and CME are offset in different directions. The example shown is from 2019-04-22, where the PEPM falls predominantly to the North, but the CME is offset South of the source.

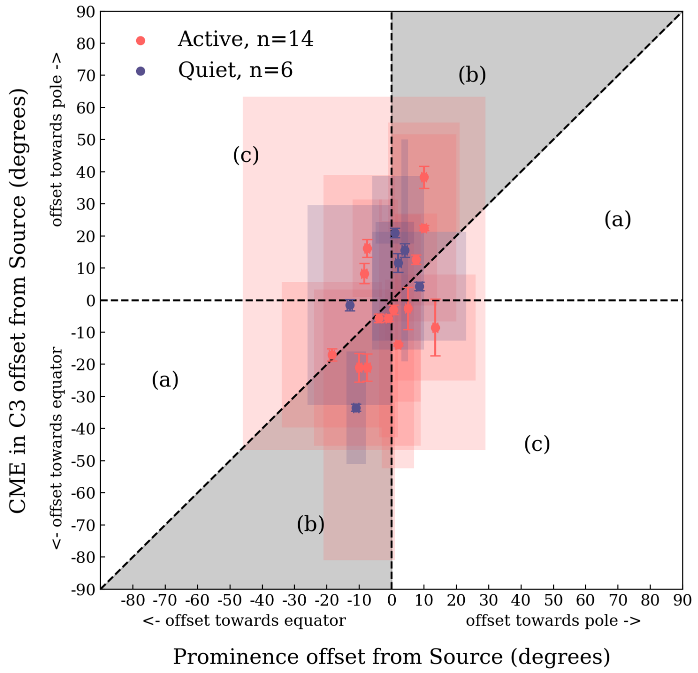

Figure 4. Comparison of CME (measured in SOHO LASCO C3) offset from source with PEPM offset from source, for both active region eruptions (pink) and quiet Sun eruptions (blue). Points representing eruptions of types (a) through (c) as defined in Figure 3 are found in their designated areas. Area (b), shaded in gray, is especially populated. The shaded boxes show the bounds in latitude of each prominence and associated CME. The vertical error bars signify the standard deviation of the three measurements taken for each CME and the horizontal error bars are based on latitude-dependent uncertanties.

For our full dataset of 20 eruptions, we compared the CME offset (as measured in SOHO LASCO C3) from the source with the PEPM offset from the source. For the two eruptions on 2015-04-28 and 2019-04-22 which were not visible in C3, we instead use their measurements in C2. The results are shown in Figure 4. The number of points appearing in each region defined by the categories from Figure 3 are shown in Table 1. The majority of points fall in or near the area formed between the diagonal $x = y$ line and the y-axis, which represents eruptions of type (b) from Figure 3 - those where the offset increases from the PEPM to the CME.

	(a)	(b)	(c)
Active (n=13)	0.0%	61.5%	38.5%
Quiet (n=8)	37.5%	50.0%	12.5%

	(a)	(b)	(c)
Percent of eruptions (n=20)	15%	55%	30%

Table 1. Percent of eruptions which fall into the three categories described in Figure 3. The majority of eruptions measured are of type (b), where the CME is offset in the same direction as, and to a greater extent than, the PEPM.

There is no difference between eruptions offset towards the equator and those offset towards the pole. A similar number of eruptions fell into each of these two categories, and eruptions of both categories followed the same trend in latitude offset.

3.2 Progression from SOHO LASCO C2 to C3

We also investigated the progression in latitude of the CME as it moves farther outward in the corona. To do this, we found the offset in latitude as before, but this time we measured the latitude of the CME at two points in its progression, at 6 $R_\odot$ from disk center in the LASCO C2 field of view and at 15 $R_\odot$ in the LASCO C3 field of view. We compared the offset in latitude from C2 to C3 with the offset in latitude from the source to the PEPM (Figure 5). We found a positive correlation between the two offsets. This continuing progression, demonstrated by eruptions that fall anywhere in the first and third quadrants, indicates that offset continues to increase from 6 $R_\odot$ to 15 $R_\odot$, at least as far out as C3. This effect could be due to continued non-radial progression and is not necessarily evidence of further deflection.

4 Discussion

4.1 Statistical interpretation of results

We measured 20 eruptions that were observed to have PEPM falling back to the Sun during an eruption with a coronal mass ejection. We observed a correlation between PEPM offset in latitude from source and CME offset from source.

To quantify this relationship, we performed a Spearman rank correlation test (Spearman, 1904) on the sample of 18 eruptions with measurements in C3. The eruptions that took place on 2015-04-28 and 2019-04-22 were too faint to be measured in C3, so we do not include them in this quantitative analysis. This statistical test provides a measure of how strongly two variables (in this case, the PEPM offset and the CME offset) are correlated without assuming any specific parametric relationship, linear or otherwise. Because our sample size is small, we used a bootstrap method, performing the statistical test on 10,000 individual samples of 14 events drawn from 18 total, with replacement. The median correlation coefficients were $\rho = 0.64$ and $R = 0.66$ for the Spearman and Pearson tests, respectively. We determined the significance level from the fraction of samples that had a Spearman correlation coefficient less than 0, the test statistic we would expect if there were no correlation. We found it to be $p = 0.0073$, meaning there is a 0.73% chance we would have observed these data if there were no correlation. We also computed a Pearson correlation coefficient by performing a linear regression on each of the 10,000 samples. We calculated a p-value in the same way as we did for the Spearman correlation,

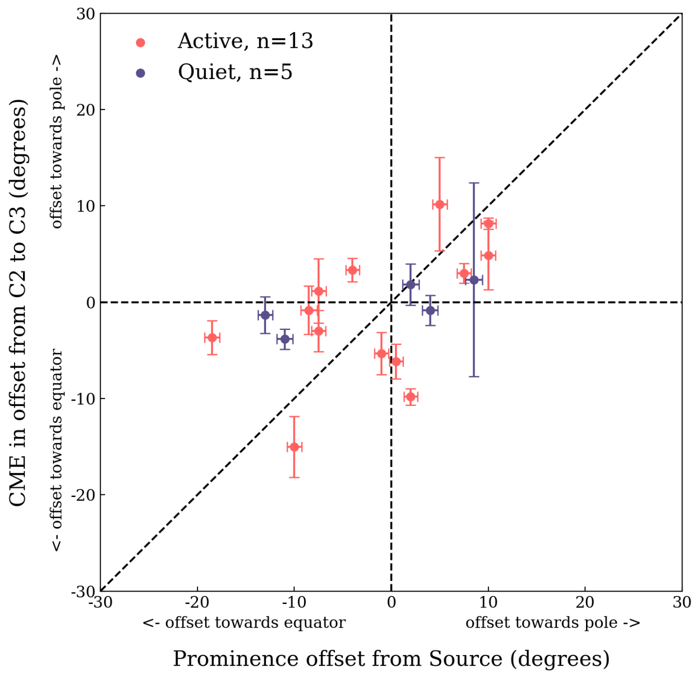

Figure 5. Comparison of CME measurement in C3 offset from CME measurement in C2 with PEPM offset from source, for both active region eruptions (pink) and quiet Sun eruptions (blue). Eruptions fall disproportionately in or near the first and third quadrants, indicating that the offset progression continues from C2 to C3.

which we determined to be $p = 0.0031$, indicating an even lower probability that we would observe this linear trend in the data if they were uncorrelated.

We observed a continued offset in CME latitude from C2 to C3, which correlated with the offset from the source to the PEPM. As we did for the comparison between the CME and PEPM offset, we used a bootstrap method and calculated Spearman and Pearson correlation coefficients for these two sets of measurements and for 10,000 samples drawn from our data. From the two distributions of coefficients, we calculate probabilities $p = 0.0213$ and $p = 0.0147$, respectively, that we would observe these data if the offset from source to PEPM and the offset from C2 to C3 were not correlated.

There is no meaningful difference in our data between eruptions offset towards the equator and eruptions offset towards the pole. A similar number of eruptions fall into each of these two categories, suggesting that the offset in latitude and the correlation between the PEPM and CME offsets in latitude is more likely a result of the local topology and dynamics of the eruptive field than a result of global magnetic structure deflecting the CME towards the equator. Cremades and Bothmer (2004), Liewer et al. (2015), Möstl et al. (2015), Sahade et al. (2020), and Mierla et al. (2022), among others, have reported deviations from radial direction that form early in the eruptive process. However, this does not exclude the possibility that the CME may undergo further deflection as it propagates. An extensive study by Kay et al. (2017) indicated that CME deflection and non-radial propagation are strongly dependent on magnetic field topology; local structures can influence the early trajectory of a CME while global structures can have an impact as the CME transits from the corona to the inner heliosphere.

4.2 Magnetic field morphological interpretation

The eruptive field changes over the course of the eruption, something that can be seen in the persistence maps of the PEPM. This material frequently falls back to the Sun under the influence of both gravity and the magnetic field. The material follows new field lines rather than fall back to the source, tracing out a changing magnetic field topology, which impacts the CME trajectory as well as the PEPM.

Persistence mapping (Thompson & Young, 2016) helps to better visualize this material as it falls back to the sun along magnetic field lines, allowing us to make diagrams of the magnetic field and how it changes over the course of the eruption. Here, we devote some time to deeper investigation of the magnetic field changes in the various types of eruption presented in this study. In Figure 6, we illustrate the prominence eruption and the changing magnetic field structure for the same three eruptions used as examples in Figures 2 and 3.

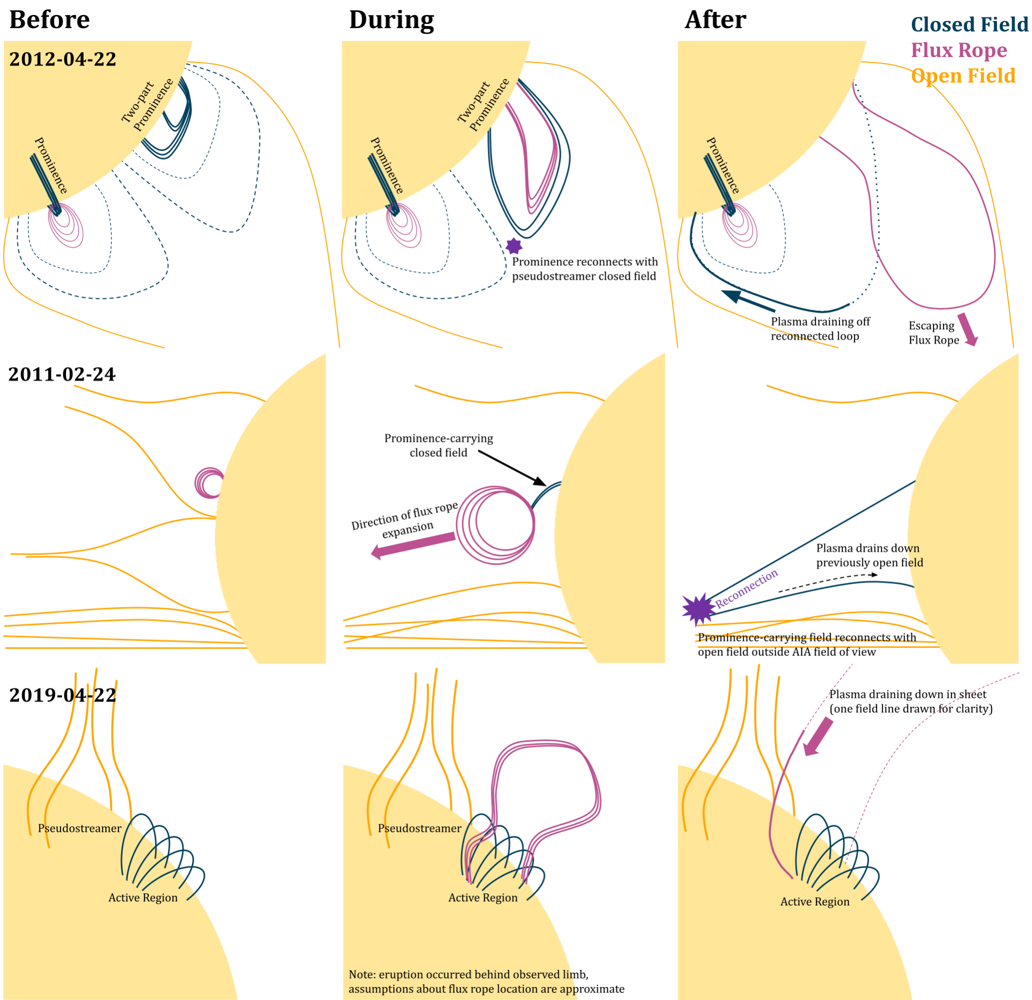

Figure 6. Magnetic field diagrams showing (from left to right) the changing magnetic field structure before, during, and after the three eruptions used as examples previously. The closed field is shown in blue, the flux rope in pink, and the open field in yellow. The eruption on 2019-04-22 occurred slightly behind the observed limb, so the assumptions about the flux rope location are approximate.

The initial, intermediate, and final configurations shown in Figure 6 were determined via comparison of SDO AIA 171 Å and 304 Å data, with occasional reference to data from the Mauna Loa Solar Observatory K-Coronagraph (MLSO KCor), which we used to confirm streamer configurations prior to some eruptions. The 171 Å data provides the clearest individual loop signatures with the minimum hot "haze" seen in other coronal filters such as 193 Å or 211 Å, which makes it the most useful channel for the assessment of magnetic configurations.

The first eruption is a pseudostreamer eruption that occurred on 2012-04-22. There were two filaments underlying a very large pseudostreamer. The one on the western limb was split into two sections, forming a "double-decker" filament. One section reconnected with the overlying closed field in the pseudostreamer and drained onto the far side of the quiescent filament to the east, while the other section continued erupting and escaped the pseudostreamer along with the CME.

The second event, from 2011-02-24, involved a flux rope which had formed under one half of a pseudostreamer adjacent to an equatorial prominence. The flux rope erupted towards the equator, pushing southward some nearby open field which was located on the other side of the low-lying prominence. Reconnection appears to occur between the open field and flux rope outside the SDO field of view, as some of the prominence plasma from the flux rope drains down onto the southern side of the equator where the open field had been before the eruption.

The final example, dated 2019-04-22, presents a contrast to this case; the flux rope expanded outwards rapidly, leaving the nearby pseudostreamer and low-lying active region fields. The cold plasma returned to the surface in a sheet after reconnecting with nearby open field from an adjacent coronal hole.

4.3 Limitations

This study only looked at the offset in latitude. With current spacecraft, which include SDO, SOHO, and STEREO A, (and STEREO B data available up until 2014), there are not enough viewpoints to make robust measurements of the PEPM or CME longitudes such that a similar study of longitude would be reliable. All of the missions used in this study were near the orbital plane of Earth, so the images were integrating along the line of sight in the longitudinal direction. Whereas a clear boundary could be identified in latitude, the longitude boundary (and its variation in time) was much less accurate to identify. With more viewpoints, particularly those out of the ecliptic plane, it will be possible to make more reliable measurements of CME velocity, which would allow for a study of whether and how velocity correlates with the latitude offset effects we observe in this study.

5 Conclusions

A comparison in the offset in latitude of the CME associated with a solar eruption from its source with the PEPM's offset from its source shows that the dynamics of the erupting prominence, not just the source location, can provide information about CME progression. The positive correlation between the offset in PEPM and CME latitude indicates that observations of remote draining of cool material during a prominence eruption can serve as a potential indicator of the extended magnetic influence of a coronal mass ejection. We find that the CME motion is typically farther from the source region than the PEPM, implying the "offset effect" increases with altitude. The PEPM can serve as a "midpoint" between the source and CME, connecting complex CME magnetic topology back to the entire lower coronal volume involved in the eruption.

These results indicate a potential diagnostic tool for CME modelers who seek to understand the extended corona involved in an eruption. Additionally, it poses a question as to why some events do exhibit PEPM and some do not, and why PEPM appear where they do. We did not observe any PEPM that fell far from the source region but were symmetric about the source location. As CME models are often centered on active region or prominence locations, PEPM can help identify additional magnetic field regions playing a role in post-eruptive processes.

Acknowledgments

Thank you to C. Richard DeVore for helpful conversations and advice. BHA's effort was funded by the Solar Dynamics Observatory mission. BJT's effort was provided through the NASA *Internal Science Funding Model* (ISFM) project "Magnetic Energy Buildup and Explosive Release in the Solar Atmosphere." EIM's research during the development of this paper was supported by an appointment to the NASA Postdoctoral Program at the NASA Goddard Space Flight Center, administered by Universities Space Research Association under contract with NASA.

Data availability. Our measurements are included in Table 2. As part of this work, we developed an implementation of the persistence mapping and time convolution mapping algorithms in Python, Hovis-Afflerbach (2023).

References

Brueckner, G. E., Howard, R. A., Koomen, M. J., Korendyke, C. M., Michels, D. J., Moses, J. D., ... Eyles, C. J. (1995, December). The Large Angle Spectroscopic Coronagraph (LASCO). *Solar Phys.*, *162*(1-2), 357-402. doi: 10.1007/BF00733434

Cremades, H., & Bothmer, V. (2004, July). On the three-dimensional configuration of coronal mass ejections. *Astron. Astrophys.*, *422*, 307-322. doi: 10.1051/0004-6361:20035776

Dissauer, K., Veronig, A. M., Temmer, M., Podladchikova, T., & Vanninathan, K. (2018, March). On the Detection of Coronal Dimmings and the Extraction of Their Characteristic Properties. *Astrophys. J.*, *855*(2), 137. doi: 10.3847/1538-4357/aaadb5

Domingo, V., Fleck, B., & Poland, A. I. (1995, December). The SOHO Mission: an Overview. *Solar Phys.*, *162*(1-2), 1-37. doi: 10.1007/BF00733425

Dudík, J., Lörinčík, J., Aulanier, G., Zemanová, A., & Schmieder, B. (2019, December). Observation of All Pre- and Post-reconnection Structures Involved in Three-dimensional Reconnection Geometries in Solar Eruptions. *Astrophys. J.*, *887*(1), 71. doi: 10.3847/1538-4357/ab4f86

Filippov, B. P. (2020). Failed Eruptions of Solar Filaments. *Astronomy Reports*, *64*(3), 272–279. doi: 10.1134/S106377292002002X

Gilbert, H. R., Holzer, T. E., Burkepile, J. T., & Hundhausen, A. J. (2000, July). Active and Eruptive Prominences and Their Relationship to Coronal Mass Ejections. *Astrophys. J.*, *537*(1), 503-515. doi: 10.1086/309030

Gopalswamy, N., Shimojo, M., Lu, W., Yashiro, S., Shibasaki, K., & Howard, R. A. (2003, March). Prominence Eruptions and Coronal Mass Ejection: A Statistical Study Using Microwave Observations. *Astrophys. J.*, *586*(1), 562-578. doi: 10.1086/367614

Hovis-Afflerbach, B. (2023, March). *berylha/persistence-mapping: Persistence Mapping for Solar Imagery [Software].* Zenodo. doi: 10.5281/zenodo.7754546

Ireland, J., Inglis, A. R., Shih, A. Y., Christe, S., Mumford, S., Hayes, L. A., ... Hughitt, V. K. (2019, November). AWARE: An Algorithm for the Automated Characterization of EUV Waves in the Solar Atmosphere. *Solar Phys.*, *294*(11), 158. doi: 10.1007/s11207-019-1505-8

Ji, H., Wang, H., Schmahl, E. J., Moon, Y.-J., & Jiang, Y. (2003). Observations of the Failed Eruption of a Filament. *The Astrophysical Journal*, *595*(2), L135–L138. doi: 10.1086/378178

Kay, C., Gopalswamy, N., Xie, H., & Yashiro, S. (2017, June). Deflection and Rotation of CMEs from Active Region 11158. *Solar Phys.*, *292*(6), 78. doi: 10.1007/s11207-017-1098-z

Lemen, J. R., Title, A. M., Akin, D. J., Boerner, P. F., Chou, C., Drake, J. F., ... Waltham, N. (2012, January). The Atmospheric Imaging Assembly (AIA) on the Solar Dynamics Observatory (SDO). *Solar Phys.*, *275*(1-2), 17-40. doi: 10.1007/s11207-011-9776-8

Liewer, P., Panasenco, O., Vourlidas, A., & Colaninno, R. (2015, November). Observations and Analysis of the Non-Radial Propagation of Coronal Mass Ejections Near the Sun. *Solar Phys.*, *290*(11), 3343-3364. doi: 10.1007/s11207-015-0794-9

Mason, E. I., Antiochos, S. K., & Vourlidas, A. (2021, jun). An Observational Study of a "Rosetta Stone" Solar Eruption. *The Astrophysical Journal Letters*, *914*(1), L8. Retrieved from `http://dx.doi.org/10.3847/2041-8213/ac0259https://iopscience.iop.org/article/10.3847/2041-8213/ac0259` doi: 10.3847/2041-8213/ac0259

Mays, M. L., Thompson, B. J., Jian, L. K., Colaninno, R. C., Odstrcil, D., Möstl, C., ... Zheng, Y. (2015, October). Propagation of the 7 January 2014 CME and Resulting Geomagnetic Non-event. *Astrophys. J.*, *812*(2), 145. doi: 10.1088/0004-637X/812/2/145

McCauley, P. I., Cairns, I. H., Morgan, J., Gibson, S. E., Harding, J. C., Lonsdale, C., & Oberoi, D. (2017, December). Type III Solar Radio Burst Source Region Splitting due to a Quasi-separatrix Layer. *Astrophys. J.*, *851*(2), 151. doi: 10.3847/1538-4357/aa9cee

Mierla, M., Inhester, B., Zhukov, A. N., Shestov, S. V., Bemporad, A., Lamy, P., & Koutchmy, S. (2022, July). Polarimetric Studies of a Fast Coronal Mass Ejection. *Solar Phys.*, *297*(7), 78. doi: 10.1007/s11207-022-02018-0

Möstl, C., Rollett, T., Frahm, R. A., Liu, Y. D., Long, D. M., Colaninno, R. C., ... Vršnak, B. (2015, May). Strong coronal channelling and interplanetary evolution of a solar storm up to Earth and Mars. *Nature Communications*, *6*, 7135. doi: 10.1038/ncomms8135

Pesnell, W. D., Thompson, B. J., & Chamberlin, P. C. (2012, January). The Solar Dynamics Observatory (SDO). *Solar Phys.*, *275*(1-2), 3-15. doi: 10.1007/s11207-011-9841-3

Petralia, A., Reale, F., Orlando, S., & Testa, P. (2016, November). Bright Hot Impacts by Erupted Fragments Falling Back on the Sun: Magnetic Channelling. *Astrophys. J.*, *832*(1), 2. doi: 10.3847/0004-637X/832/1/2

Sahade, A., Cécere, M., & Krause, G. (2020, June). Influence of Coronal Holes on CME Deflections: Numerical Study. *Astrophys. J.*, *896*(1), 53. doi: 10.3847/1538-4357/ab8f25

Schmieder, B., Démoulin, P., & Aulanier, G. (2013). Solar filament eruptions and their physical role in triggering coronal mass ejections. *Advances in Space Research*, *51*(11), 1967–1980. doi: 10.1016/j.asr.2012.12.026

Spearman, C. (1904). The proof and measurement of association between two things. *The American Journal of Psychology*, *15*(1), 72–101.

SunPy Community, Barnes, W. T., Bobra, M. G., Christe, S. D., Freij, N., Hayes, L. A., ... Dang, T. K. (2020, February). The SunPy Project: Open Source Development and Status of the Version 1.0 Core Package. *Astrophys. J.*, *890*(1), 68. doi: 10.3847/1538-4357/ab4f7a

Susino, R., Bemporad, A., & Dolei, S. (2014, July). Three-dimensional Stereoscopic Analysis of a Coronal Mass Ejection and Comparison with UV Spectroscopic Data. *Astrophys. J.*, *790*(1), 25. doi: 10.1088/0004-637X/790/1/25

Thompson, B. J., & Young, C. A. (2016, July). Persistence Mapping Using EUV Solar Imager Data. *Astrophys. J.*, *825*(1), 27. doi: 10.3847/0004-637X/825/1/27

Tripathi, D., Reeves, K. K., Gibson, S. E., Srivastava, A., & Joshi, N. C. (2013). SDO/AIA observations of a partially erupting prominence. *Astrophysical Journal*, *778*(2), 1–7. doi: 10.1088/0004-637X/778/2/142

Uritsky, V. M., Thompson, B. J., & DeVore, C. R. (2022, August). Remote Sensing of Coronal Forces during a Solar Prominence Eruption. *Astrophys. J.*, *935*(1), 47. doi: 10.3847/1538-4357/ac74b4

van Driel-Gesztelyi, L., Baker, D., Török, T., Pariat, E., Green, L. M., Williams, D. R., … Malherbe, J. M. (2014, June). Coronal Magnetic Reconnection Driven by CME Expansion—the 2011 June 7 Event. *Astrophys. J.*, *788*(1), 85. doi: 10.1088/0004-637X/788/1/85

van Ballegooijen, A. A., & Martens, P. C. H. (1989). Formation and eruption of solar prominences. *The Astrophysical Journal*, *343*(1967), 971. doi: 10.1086/167766

Wold, A. M., Mays, M. L., Taktakishvili, A., Jian, L. K., Odstrcil, D., & MacNeice, P. (2018, March). Verification of real-time WSA-ENLIL+Cone simulations of CME arrival-time at the CCMC from 2010 to 2016. *Journal of Space Weather and Space Climate*, *8*, A17. doi: 10.1051/swsc/2018005

Zheng, R., Chen, Y., Wang, B., & Song, H. (2020, May). An Extreme Ultraviolet Wave Associated with a Solar Filament Activation. *Astrophys. J.*, *894*(2), 139. doi: 10.3847/1538-4357/ab863c

Eruption Date	Region Type	Source		PEPM		C2		C3	
		N	S	N	S	N	S	N	S
2011-02-24	Active	16 ± 1	13 ± 1	13 ± 1	-21 ± 1	20.0 ± 4.4	-17.7 ± 1.2	21.7 ± 4.0	-26.7 ± 1.5
2011-06-07	Active	-19 ± 1	-25 ± 1	27 ± 1	-54 ± 1	21.0 ± 1.0	-83.3 ± 3.8	27.7 ± 4.0	-88.3 ± 3.8
2011-08-11	Active	19 ± 1	14 ± 1	28 ± 1	-10 ± 1	21.7 ± 4.2	-33.0 ± 1.7	22.3 ± 6.7	-31.3 ± 5.0
2011-10-25	Quiet	-8 ± 1	-10 ± 1	18 ± 1	-10 ± 1	20.3 ± 4.9	-38.0 ± 0.0	24.7 ± 4.7	-39.67 ± 0.58
2011-11-17	Active	28 ± 1	28 ± 1	48 ± 1	28 ± 1	64.33 ± 0.58	20.3 ± 1.2	79.7 ± 1.5	21.3 ± 2.1
2011-11-22	Quiet	41 ± 1	26 ± 1	44 ± 1	31 ± 1	88.3 ± 1.5	11.33 ± 0.58	91.0 ± 5.3	7.0 ± 2.0
2012-01-02	Active	8 ± 1	5 ± 1	9 ± 1	-16 ± 1	53.3 ± 2.1	-52.33 ± 0.58	47.0 ± 6.6	-76.0 ± 4.4
2012-03-15	Active	21 ± 1	20 ± 1	42 ± 1	19 ± 1	69.7 ± 5.5	38.3 ± 4.6	76.3 ± 9.0	41.3 ± 1.2
2012-04-22	Quiet	-32 ± 1	-47 ± 1	-26 ± 1	-70 ± 1	-10 ± 34	-73.3 ± 2.5	-19.3 ± 2.1	-68.3 ± 4.0
2012-06-27	Quiet	43 ± 1	41 ± 1	53 ± 1	35 ± 1	75.33 ± 0.58	28.3 ± 1.5	81.7 ± 1.5	25.7 ± 7.6
2012-09-22	Active	-5 ± 1	-7 ± 1	-2 ± 1	-14 ± 1	28.7 ± 3.5	-32.7 ± 2.1	47.3 ± 1.5	-31.67 ± 0.58
2014-01-01	Active	-14 ± 1	-21 ± 1	-15 ± 1	-30 ± 1	25.3 ± 3.8	-35.0 ± 1.0	17.7 ± 9.0	-47.7 ± 7.4
2014-04-19	Active	12 ± 1	8 ± 1	9 ± 1	-4 ± 1	49.0 ± 3.0	9.3 ± 5.5	43.3 ± 4.2	9.0 ± 9.6
2014-09-12	Active	-6 ± 1	-14 ± 1	-4 ± 1	-17 ± 1	-1.67 ± 0.58	-24.7 ± 5.0	6.3 ± 2.9	-20.3 ± 3.2
2015-02-08	Active	10 ± 1	7 ± 1	6 ± 1	3 ± 1	17.3 ± 8.0	-18.3 ± 5.5	17.0 ± 3.5	-11.3 ± 2.9
2015-04-28	Quiet	20 ± 1	5 ± 1	27 ± 1	0 ± 1	44.3 ± 5.7	22.7 ± 2.5		
2018-03-31	Active	-7 ± 1	-9 ± 1	-8 ± 1	-23 ± 1	-0.3 ± 1.5	-35.0 ± 1.0	-5.3 ± 4.0	-36.0 ± 1.0
2019-04-22	Active	15 ± 1	13 ± 1	41 ± 1	14 ± 1	24.7 ± 4.9	-12.7 ± 18.0		
2019-05-03	Active	15 ± 1	12 ± 1	17 ± 1	8 ± 1	45.7 ± 1.5	-19.3 ± 5.8	46.3 ± 1.5	-30.7 ± 2.1
2020-07-05	Quiet	-33 ± 1	-44 ± 1	-19 ± 1	-36 ± 1	16.7 ± 4.9	-34.3 ± 3.5	18.0 ± 1.7	-28.0 ± 3.6

Table 2. Data for all 20 eruptions, including eruptive region types and measurements in degrees.